



Article

Differential Entropy: An Appropriate Analysis to Interpret the Shape Complexity of Self-Similar Organic Islands

Stefano Chiodini ^{1,2} , Pablo Stoliar ³, Pablo F. Garrido ⁴ and Cristiano Albonetti ^{1,*} 

¹ Consiglio Nazionale delle Ricerche—Istituto per lo Studio dei Materiali Nanostrutturati (CNR-ISMN), Via P. Gobetti 101, 40129 Bologna, Italy; Stefano.Chiodini@iit.it

² Center for Nano Science and Technology, Fondazione Istituto Italiano di Tecnologia, Via G. Pascoli 70, 20133 Milan, Italy

³ National Institute of Advanced Industrial Science and Technology (AIST), Tsukuba 305-8565, Japan; p.stoliar@aist.go.jp

⁴ Departamento de Física de Aplicada, Facultad de Física, Universidade de Santiago de Compostela, E-15782 Santiago de Compostela, Spain; Pablo.Fernandez@usc.es

* Correspondence: cristiano.albonetti@cnr.it

Abstract: Differential entropy, along with fractal dimension, is herein employed to describe and interpret the shape complexity of self-similar organic islands. The islands are imaged with in situ Atomic Force Microscopy, following, step-by-step, the evolution of their shape while deposition proceeds. The fractal dimension shows a linear correlation with the film thickness, whereas the differential entropy presents an exponential plateau. Plotting differential entropy versus fractal dimension, a linear correlation can be found. This analysis enables one to discern the 6T growth on different surfaces, i.e., native SiO_x or 6T layer, and suggests a more comprehensive interpretation of the shape evolution. Changes in fractal dimension reflect rougher variations of the island contour, whereas changes in differential entropy correlates with finer contour details. The computation of differential entropy therefore helps to obtain more physical information on the island shape dependence on the substrate, beyond the standard description obtained with the fractal dimension.

Keywords: in situ imaging; atomic force microscopy; differential entropy; fractal dimension; sexithiophene; Ehrlich-Schwoebel barrier



Citation: Chiodini, S.; Stoliar, P.; Garrido, P.F.; Albonetti, C.

Differential Entropy: An Appropriate Analysis to Interpret the Shape Complexity of Self-Similar Organic Islands. *Materials* **2021**, *14*, 6529. <https://doi.org/10.3390/ma14216529>

Academic Editor: Oleg Igorevich Lebedev

Received: 15 September 2021
Accepted: 25 October 2021
Published: 29 October 2021

Publisher's Note: MDPI stays neutral with regard to jurisdictional claims in published maps and institutional affiliations.



Copyright: © 2021 by the authors. Licensee MDPI, Basel, Switzerland. This article is an open access article distributed under the terms and conditions of the Creative Commons Attribution (CC BY) license (<https://creativecommons.org/licenses/by/4.0/>).

1. Introduction

The failure of standard atomistic theories to completely describe Organic Thin Films (OTFs) has already shone light on the richer physics of organic molecular systems. The growth of OTFs, due to their complex shapes and internal degrees of freedom, gives rise to peculiar behaviours, such as rapid roughening [1], roughening transition [2], and thickness dependent lattice unit vectors [3]. The Ehrlich-Schwoebel barrier (ESB) [4,5] has been recognized as the main factor causing a layer-by-layer, or pyramidal, growth of the film [6], but the lack of a standard theory of the molecular film growth makes its evaluation difficult. In the literature, only a few examples of molecular simulations [7,8] and experimental measurements [6,9,10] provide, or attempt to provide, insights on its calculation.

To overcome such limitations, the morphology of OTFs has been deeply investigated, looking for the building blocks of the molecular film growth [11]. Most of the molecules employed in these experiments are small organic molecules deposited on weakly interacting substrates, e.g., SiO₂ [12]. Such configurations are fundamental in the fabrication of organic electronic devices [13,14] where a strong correlation between morphology and electrical performance was extensively proved [15–18].

In general, OTFs on SiO₂ follow the Stranski-Krastanov (SK) growth mode [19,20], a mixed scenario involving both Frank–Van der Merwe (FM, two-dimensional films) and Volmer–Weber growth modes (VW, three-dimensional films) [21]. At the SiO₂ interface, the

OTF is characterized by two or three complete FM layers [21]. These layers, also known as monolayers (MLs), are complete and composed of quasi upright standing molecules [22–27]. After that, the growth switches to VW and three-dimensional structures form [19].

In the past, scaling laws were employed to study, statically [1,28,29] and dynamically [19,26,30,31], the morphological evolution of OTFs for increasing thickness, proving the self-affinity of the OTFs surface profile [10,32–36].

On the other hand, a geometrical approach is used when OTFs are ultrathin (≤ 1 ML), i.e., at the SiO₂ interface. In this initial stage, the average area, superficial density, surface coverage, and critical size of mounds and/or islands were measured [37–42]. Their self-affinity was studied with the fractal dimension [43,44], thus connecting the geometrical shape of mounds and/or islands to their growth evolution in the sub-monolayer regime [45–50]. Such a geometrical shape, as originally explained by Ehrlich [4], is connected to the ESB, and thus to the fractal dimension. On this basis, Hlawacek et al. [6] have experimentally measured the ESB for para-sexiphenyl (6P) mounds, suggesting, however, that the inorganic growth theory, applied to organic growth, needs to take into account some additional effects dependent on the type of molecule employed.

To correctly describe the island border complexity, information entropy appears to be the right mathematical concept. This approach has already been used in computer vision where information entropy allows the recognition of two-dimensional shapes (or patterns) through their complexity [51–53].

Originally adopted by Shannon [54], the term ‘information entropy’ can generate misunderstandings and confusion. He defines entropy as a measure of the uncertainty of data in an information channel, so the highest value corresponds to “missing information” [55]. As reported in the literature [56,57], this mathematical entropy is not correlated to the thermodynamic one, although the latter one has been successfully applied to both theoretical [58–60] and experimental [61] statistical mechanics.

In modern science, information entropy is often associated with the fractal dimension, with both being measurements of complexity. Among others, applications can be found in geology [62], biology [63], and medicine [64]. In the field of OTFs, only in a study of fullerene film fractal dimension and entropy were singly calculated [65].

This work aims to fill this gap by measuring island shape complexity through the differential entropy, i.e., the information entropy extended to continuous variables. Such entropy is measured by evaluating the probability distributions of local angles along the island contours [52]. This analysis increases the classification efficiency of the island shapes beyond fractal dimension. Mathematical relationships linking differential entropy and fractal dimension can help to discern growth phenomena through geometrical parameters [66].

Such measurements are performed with in situ Atomic Force Microscopy (AFM) that allows step-by-step imaging of the growth evolution [19]. Thus, the shape complexity can be measured with a high accuracy of film thickness. To our knowledge, this is the first example reported up to now where the shape complexity is monitored in situ, in UHV, and with time.

2. Materials and Methods

2.1. Sample Preparation

The growth of 6T OTFs on native SiO_x (Boron doped, *p*-type, 5–10 Ω·cm) was performed subliming 6T polycrystalline powder (Sigma-Aldrich, used as received) through an Organic Material Effusion (OME) Knudsen cell (Dr. Eberl MBE-Komponenten GmbH, Weil der Stadt, Germany) in Ultra-High Vacuum (UHV—base pressure 2×10^{-10} mbar). Two experiments at different substrate temperatures T_S were performed, viz. 25 and 50 °C. The deposition flux was kept constant to $\sim 1 \text{ \AA} \cdot \text{min}^{-1}$. The OTF thickness is measured in MLs where a monolayer (ML) is a layer of ordered and packed molecules almost orthogonal to the SiO_x surface that completely covers it ($\Theta = 1$). Accordingly, each layer composing the OTF can be expressed in terms of an equivalent surface coverage Θ [15]. The maximum thickness was fixed to 6.5 ML, as measured at 25 °C, where molecular desorption can be

considered negligible [19]. In the case of 6T, each monolayer corresponds to a thickness of 2.4 nm [22], so the maximum OTF thickness is 16.9 nm.

2.2. AFM Imaging

The growth of 6T OTFs was followed in situ and step-by-step with a commercial UHV system (Omicron GmbH, Taunusstein, Germany), combining an OME Knudsen cell and an AFM microscope (Omicron GmbH, Taunusstein, Germany, VT-UHV SPM XA 50–500 K). Relatively stiff cantilevers (Nanosensors, resonance frequency of ~300 kHz, and spring constant of ~10 N·m⁻¹) were employed in Non-Contact AFM (NC-AFM). Sequential AFM images were taken every ~0.25 ML, i.e., every four minutes of deposition. The scan area was selected to 6 × 6 μm², the largest possible scan size granting stable NC-AFM images. T_S was set to 25 and 50 °C to provide a statistically relevant number of islands because, as shown in a previous work [19], higher T_S do not provide enough islands. The same work reports also two different populations of islands at early stage of the growth: smaller islands with a high density and bigger islands with a low density [19,67]. The oblique position of the OME cell, together with the non-hermetic closure of its shutter, are responsible for such bimodal growth. In fact, when the inclination angle of the OME cell, with respect to the unit vector normal to the substrate plane, is larger than 40° (in our case 60°), the substrate collects molecules from the lobe-shaped vapour clouds coming from larger emission angles (see Figure 43 in reference [68]), a phenomenon increased by the distribution of the powder along the crucible wall [69]. In this work, bigger islands at each T_S are excluded from the morphological analysis.

2.3. Image Processing and Data Analysis

As proposed by Mandelbrot [70], the perimeter–area (P–A) relationship can be applied to determine the fractal dimension D_f of the perimeter-line of the islands, analysing not an individual island but a group of them. In order to do that, fractality should hold in a “wide enough” size-range [71], where two orders of magnitude are usually considered wide enough. Through this method, 6T islands imaged by AFM on a large scan-range (viz 20 × 20 μm²) were demonstrated to be a set of self-similar objects [29]. Due to both our limited scan range (6 × 6 μm²) and the average island size for each T_S , the images of this work can yield erroneous D_f values if calculated with the standard P–A method because the size-range of fractality is not “wide enough” and the number of islands is limited [72]. To overcome this problem, D_f was calculated with the box counting method [73], for which the size-range of images in pixels, i.e., 1024 × 563 px², is “wide enough” to hold fractality on, at least, three orders of magnitude.

The topographic images were processed with Gwyddion software [74]: (1) data were levelled by the mean plane subtraction; (2) paraboloidal background was removed; (3) rows were aligned by means of the median of differences; (4) horizontal scars were corrected; (5) mean values filter (3 × 3 px²) was applied to remove any possible topographic artefact.

Amongst all the images that follow the growth step-by-step (at least four images for each ML), only those below the aggregation regime for each ML were analysed (partial surface coverage $\Theta_p \sim 0.5 \text{ ML} + n$ where $n = 0, 1, 2,$ and 3 ML) [75]. This choice avoids an erroneous fractal dimension calculus with the lacunarity method [43] and satisfies the condition of well-separated islands. Accordingly, the islands are firstly marked by thresholding, and the selected islands are then filtered by area in order to remove larger islands induced by the bimodal growth (see Figure 1a). The resulting mask is extracted and used to statistically evaluate the average area of the islands, thus determining the largest box size (closeness power of 2) employed in the box counting method (see Figure 1b, see Supplementary Materials). As required for fractal calculus in ImageJ [76], the mask is changed to 8 bit and binarized. Then, the fractal dimension is calculated by using power of 2 box sizes, i.e., $2^0, 2^1, 2^2, \dots$, thus reducing the error in D_f (Figure 1c) [73].

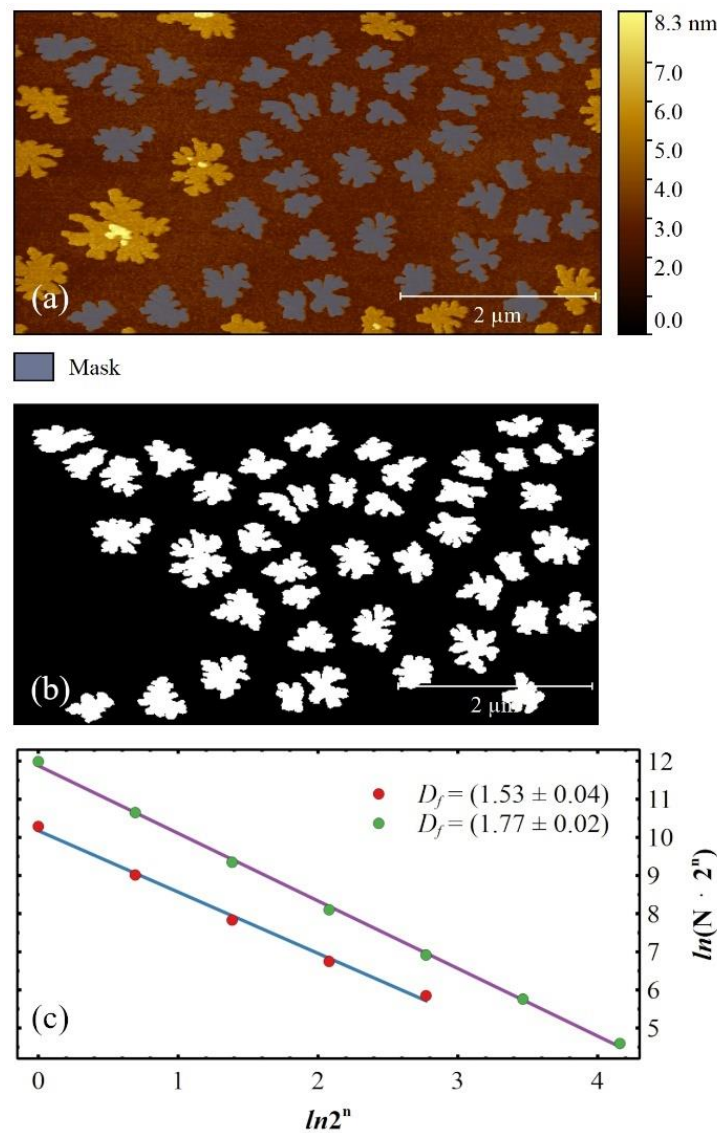


Figure 1. (a) Typical AFM image of 6T islands grown by Organic Molecular Beam Deposition (OMBD) on native SiO_x in UHV ($\Theta = 1.5$ ML and $T_S = 50$ °C). The bimodal growth is highlighted by both thresholding and filtering procedures (east bay coloured mask); (b) Binarized extracted mask with an average islands area of ~ 2850 px², correspondent to a box size of ~ 55 px, closeness to 64 px, i.e., 2^6 px as a power of 2; (c) Fractal dimension D_f calculated for seven box sizes: $2^0, 2^1 \dots 2^6$ px (green dots). The natural logarithm (\ln) of the number of covering boxes (N) of each size times the length of a box edge (2^n) is plotted against the $\ln(2^n)$. A straight-line with a negative slope B results, and D_f is calculated as $1 - B$. In the x -axis, the box size changes a few units, i.e., $\ln(2^6) = 6 \cdot \ln 2 \sim 4.16$, while in the y -axis, N spans 5 orders of magnitude, from few units for 2^6 to $\sim 1.6 \times 10^5$ for 2^0 . The D_f is affected by the average area of 6T islands, returning a smaller value of D_f for a smaller average area (red dots, $\Theta = 1.08$ ML and $T_S = 50$ °C).

To go a step further, the fractal dimension, which, at least in OTF theories, appears to be only a geometrical parameter, the differential entropy S of islands is introduced [77] (see Supplementary Materials):

$$S = - \int_0^{180} p(\alpha) \ln[p(\alpha)] d\alpha \quad (1)$$

where the continuous random variable α , with probability density function (pdf) $p(\alpha)$, ranges from 0 to 180° (degree).

The differential entropy extends the Shannon entropy concept to a continuous probability distribution [78]. All histograms generated and analysed in this study have a consistent number of bins set to 180 (bin size $\Delta\alpha = 1^\circ$), hence S ranges from 0 to ~ 5.2 nats (see Supplementary Materials).

In order to calculate S , AFM images were firstly segmented by ad hoc image segmentation procedure consisting of three steps (Figure 2b–d, see Supplementary Materials). The original AFM image (Figure 2a) is firstly binarized by using the mask procedure described above, obtaining a two-level bitmap image with a black background and white islands (Figure 2b). The contour of the islands is then traced by using the “trace bitmap” function of Inkscape software [79] (Figure 2c). This function detects island contours, “tracing” them using a series of lines and cubic Bezier curves. Finally, traced contours were turned into polygonal chains composed of small segments with “adapted” lengths (Figure 2d, see Supplementary Materials).

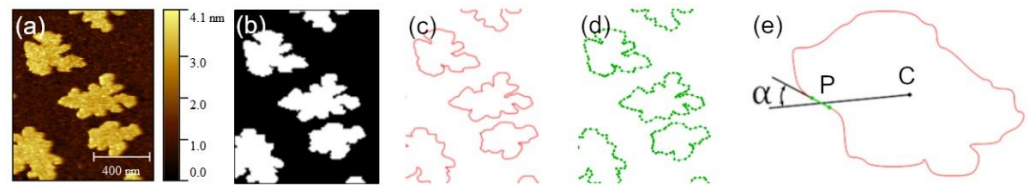


Figure 2. Graphical steps to obtain polygonal chains describing island contours. (a) Original AFM image; (b) two-levels bitmap image of well-identified islands are clearly; (c) Contours of the islands traced as a series of lines and Bezier curves; (d) Polygonal chains describing island contours (dots are vertexes of linear segments). For graphical purposes, linear segments of polygonal chains are 20 times lower than those used for calculating S . (e) Angle α between a segment centre of the island contour (green line with centre P) and the radial line to the centroid C of the island.

Once islands are segmented, α for each segment is obtained by measuring the angle between the semi straight line joining the centre C of the island and the segment centre P (Figure 2e, see Supplementary Materials). Lastly, the differential entropy S of Equation (1) is calculated as the pdf area of the bar chart, where $p(\alpha)$ is the ratio between the sum of segment lengths with angle α and the island contour length, normalized with respect to the bin $\Delta\alpha$ (see Supplementary Materials).

3. Results

Figure 3 shows AFM images of 6T OTFs deposited on native silicon oxide [37]. For each T_S , i.e., 25 (left column, a–d) and 50 °C (right column, e–h), an image for each layer is represented at roughly half of the layer growth and up to 4 ML at most. The sequence of AFM images illustrates the step-by-step and in situ evolution of OTFs.

At each T_S , the same $6 \times 6 \mu\text{m}^2$ region was scanned enabling to follow the growth of every single 6T island (cp. to Section 2.2). The column on the left shows the 25 °C case (a–d) while the column on the right corresponds to the 50 °C case (e–h). Several observations can be done: (i) regardless T_S , OTFs grew in a SK growth mode; (ii) at 25 °C, 6T islands have an average area smaller than at 50 °C [80], (iii) the island superficial density is clearly affected by the temperature, with a higher density at 25 °C with respect to 50 °C [38,40], and (iv) the island shape at 50 °C appears to be more dendritic with respect to 25 °C. These results agree to the OTF theory [29,81], confirming the proper OTFs preparation by OMBD in UHV.

As described in Section 2.2, the bimodal growth is caused by the oblique position of the OME cell, and its effect is particularly evident in the first ML (Figure 3a,e). Smaller islands with higher superficial density are considered consistent to the 6T aggregates formed by OMBD in UHV, thus larger islands are excluded from the morphological analysis (cp. to Figure 1a).

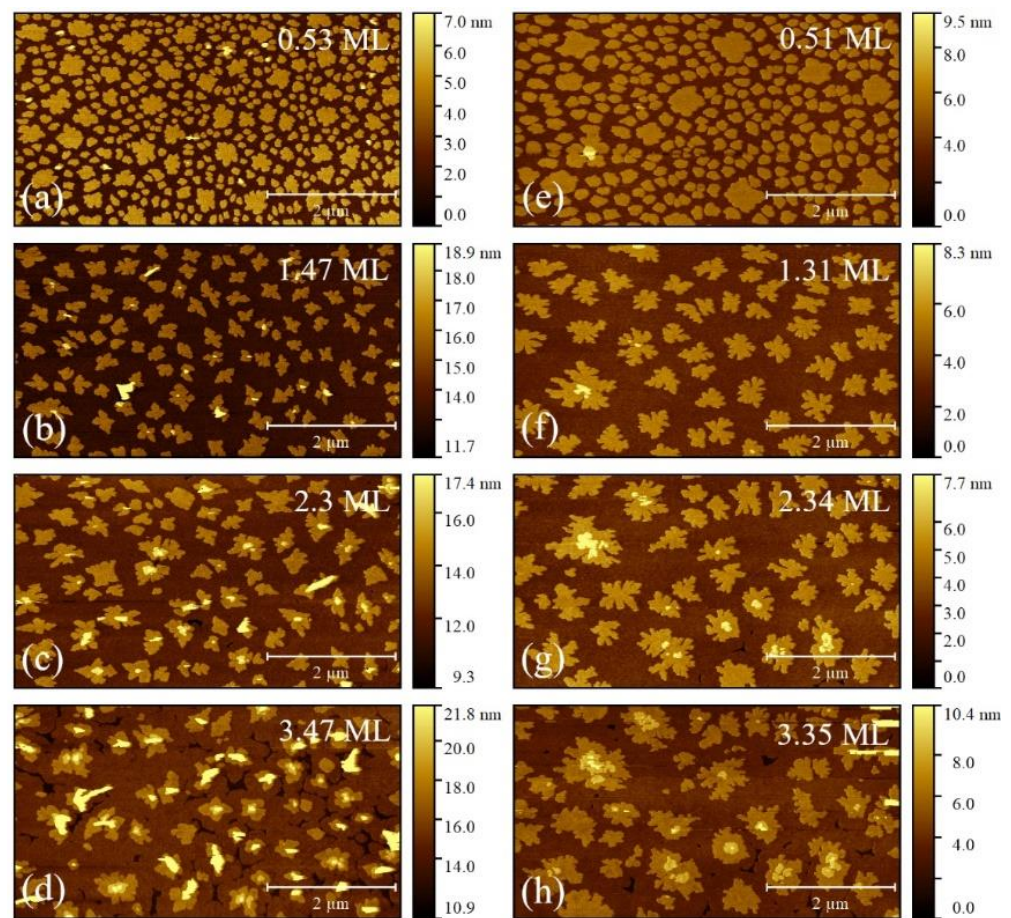


Figure 3. AFM images of 6T islands grown with OMBD in UHV on native silicon oxide at 25 °C (a–d) and at 50 °C (e–h). The surface coverage Θ for each AFM image is reported in the top-right corner. At each image, the same region was scanned, and the morphological evolution of OTFs can be followed along with the increasing coverage, up to the 4th ML. For graphical purposes, AFM images are cropped to $6.0 \times 3.3 \mu\text{m}^2$, whereas some images (b–d) present a z-scale range starting from a height $\neq 0$ nm because the underlying MLs are incomplete.

Amongst several morphological parameters, the fractal dimension D_f is commonly used to quantify the average island shape [29,44,82]. Specifically, D_f is expected to be close to 1 for a perfectly round island [83], while it increases towards 2 for islands with highly ramified contours [84], passing through randomly ramified aggregates grown by the Diffusion Limited Aggregation (DLA) condition ($D_f = 1.71$) [85]. Taking Figure 4 of reference [86] as a reference, the island shape is termed compact ($D_f \rightarrow 1$), dendritic ($1 < D_f < 2$) or fractal ($D_f \sim 1.71$) when its shape is regular (e.g., a circle) [87], has (few or many) branches characterizing preferred growth directions [44], or is highly randomly ramified [82,88], respectively. In situ AFM imaging enables to follow step-by-step the OTF growth [19], hence D_f versus Θ .

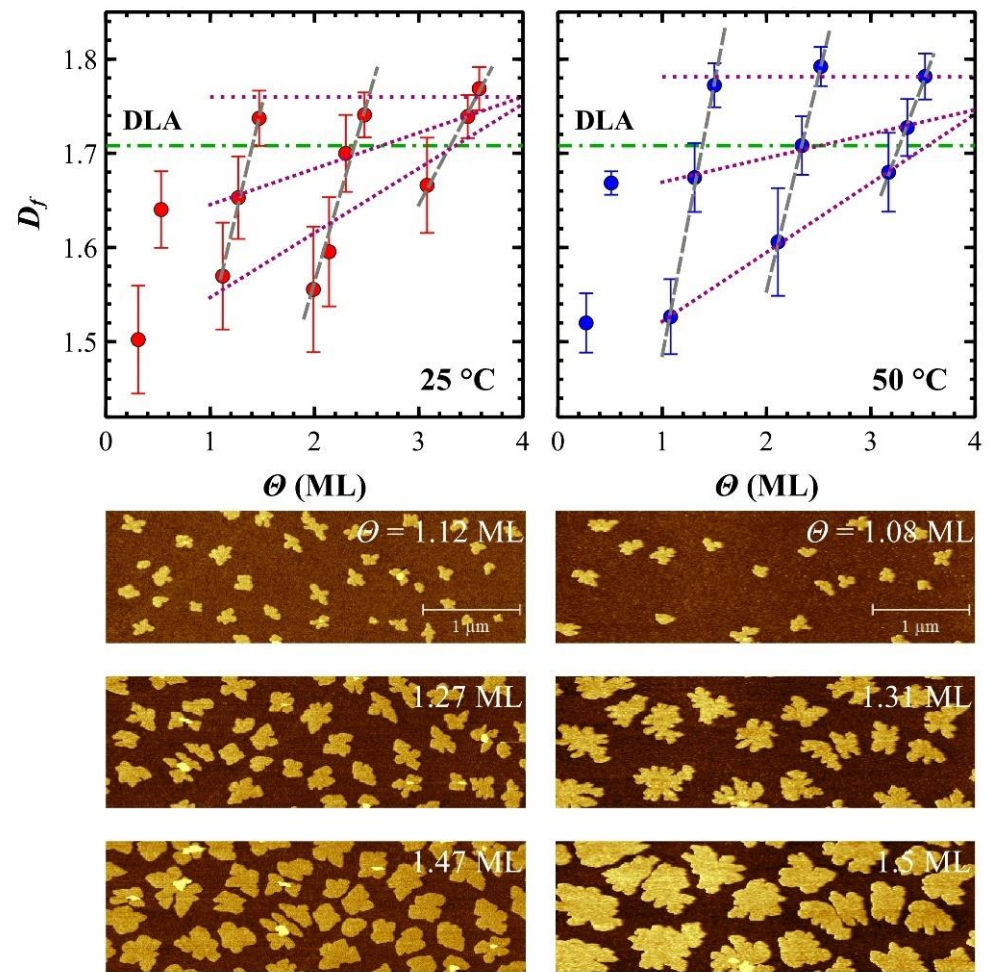


Figure 4. Fractal dimension plots for 25 °C (**left**) and 50 °C (**right**) referred to the DLA limit (dashed-dot lines). Illustrative examples of in situ AFM images for increasing partial coverage Θ_p below the aggregation regime ($\Theta_p < n + 0.5$ where $n = 0, 1, 2,$ and 3) for 25 °C (**left**) and 50 °C (**right**).

Due to the limits discussed in Section 2.3, D_f of the 6T islands is calculated by using the box counting method [73]. The fractal dimension increases linearly versus Θ within each ML (see dashed lines in Figure 4). Its value shifts from compact islands with D_f ranging from 1.5 to 1.6, like pentacene islands [89], to dendritic ones with $D_f \sim 1.75$ that is close to 1.71, the mathematical limit characterizing fractal islands formed by DLA (see horizontal dashed-dotted line in Figure 4) [43,90]. This effect is particularly evident for sequential in situ AFM images at 50 °C where the same islands evolve from smooth to dendritic shapes (see Figure 4, right column). The direct visual comparison between AFM images at 25 and 50 °C also explains why D_f is lower at 25 °C than at 50 °C for any Θ : lower T_S promoted islands with smoothed shapes.

The slopes of linear fits, below the aggregation regime, decrease for increasing MLs, suggesting an evolution of island shape versus MLs. The first ML is excluded from linear fitting since it is described by only two Θ points. This trend can be explained by following the evolution of D_f for comparable partial surface coverage Θ_p , e.g., ~ 1.3 ML, ~ 2.3 ML, and ~ 3.3 ML (see dotted lines in Figure 4). The progressive linear increasing of D_f for increasing Θ_p causes an increase of D_f at the initial Θ_p , i.e., ~ 1.1 ML, ~ 2.1 ML, and ~ 3.1 ML, while D_f is constant to ~ 1.75 for Θ_p just below the aggregation regime of each ML, i.e., ~ 1.5 ML, ~ 2.5 ML, and ~ 3.5 ML. In reason of that, a progressive slope decreasing for increasing MLs is observed. This trend is independent from T_S because, although D_f at 50 °C is larger than at 25 °C, D_f versus Θ slopes decrease linearly with the same slope (see Supplementary Materials).

The differential entropy S provides additional information on the geometrical evolution of 6T islands for increasing deposited molecules.

In the information theory, the Shannon entropy SE of a discrete random variable is the average level of uncertainty inherent to the variable possible outcomes [54] (see Supplementary Materials). The minimum uncertainty occurs for a known event (probability $p = 1$), so the entropy SE is zero bits. Conversely, the maximum uncertainty occurs for equiprobable events with $p = n^{-1}$ where n is the number of bins, hence SE is at its maximum. Other values of p give different entropies S between these two limits.

The differential entropy S extends the Shannon entropy concept to a continuous variable, thus the probability histogram turns into a probability distribution function (pdf) that characterizes the amount of information contained in the continuous variable [91]. In our case, the probability density function $p(\alpha)$ (see Equation (1)) describes the probability to find the angle α within the range $[0, 180]$ degree. Besides the difference between discrete and continuous variables, SE measures an absolute (information) entropy, whereas S measures a relative entropy, i.e., a change of uncertainty [92]. For instance, Fhionnlaioich et al. [93] have used SE to characterize the size distributions of monodisperse nanoparticles. Nevertheless, they classify the nanoparticle population into a set of categories computing (absolute) SE . Conversely, angle distributions computed from AFM images in these experiments are treated as a continuous variable, returning a (relative) differential entropy S . Specifically, S measures the relative change of islands' entropy as the film grows, but it cannot provide any conclusion on its absolute value.

As described in Section 2.3, α pdfs obtained analysing AFM images show characteristic features (see Figure S7 in Supplementary Materials): (i) compact islands are characterized by high angular information with a Gaussian distribution and a lower S (see Figure 5, pdf on the left); (ii) dendritic islands are characterized by low angular information with a *quasi*-rectangular distribution, i.e., angles α are *quasi*-equiprobable, and a higher S (see Figure 5, pdf on the right); (iii) regardless of Θ and T_S , pdfs are characterized by a constant baseline (blue dashed line in both pdfs); (iv) pdfs at 25 °C mainly show a single Gaussian and, sometimes, a convolution of two, while pdfs at 50 °C are balanced between single Gaussian and *quasi*-rectangular distributions. This trend suggests that 6T islands are more compact at 25 °C with respect to the ones at 50 °C.

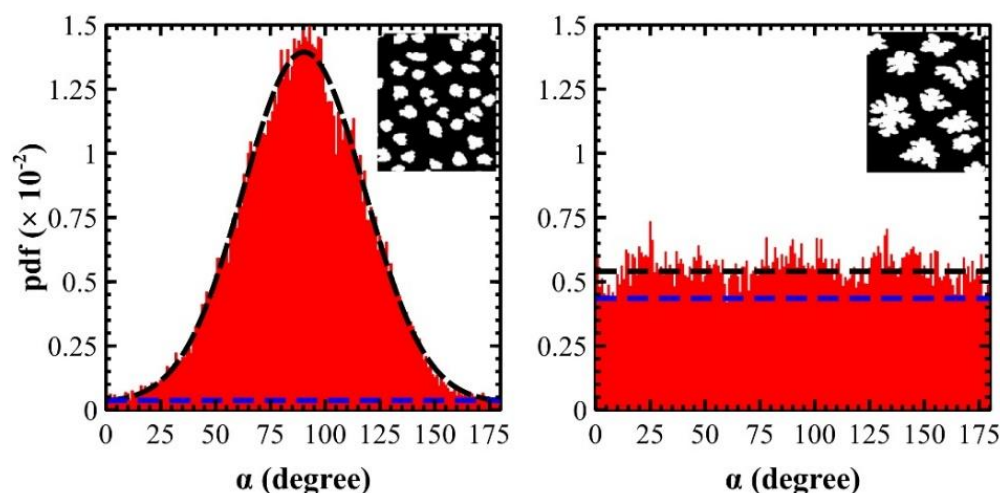


Figure 5. Illustrative pdf plots for compact (left) and dendritic (right) islands grown at 50 °C. The former is formed at the early stage of the growth ($\Theta = 0.28$ ML), the latter at the first deposition step after the first ML ($\Theta = 1.29$ ML). Both curves have a constant baseline of 0.00028 and 0.0045 (dashed blue lines) for compact and dendritic islands, respectively (see inset images). At 25 °C, Gaussian curve perfectly fits the pdf (dashed black lines) while the *quasi*-rectangular distribution shows a probability fluctuation around 0.0055.

In most cases, pdfs can be fitted with Gaussian (left panel in Figure 5, dashed black fit) and uniform functions (right panel in Figure 5, $y = a$ where a is the constant probability—dashed black line). The differential entropy S (in nats) is $\frac{1}{2}\ln[(2\cdot\pi\cdot e)\cdot\sigma^2]$ and $-a\cdot\ln(a)\cdot(x_f - x_i)$ for Gaussian and uniform functions [94], respectively. Specifically, σ is the standard deviation of the Gaussian distribution, whereas $(x_f - x_i)$ is defined by integral limits of Equation (1), i.e., 180. In sporadic cases, pdf is the convolution of two Gaussians and $S\sim\frac{1}{2}\ln[(2\cdot\pi\cdot e)\cdot\sigma^2] + A$, where A is a constant defined in reference [77] (By applying these functions to pdfs of Figure 5, S is: (left panel) $\frac{1}{2}\ln[(2\cdot\pi\cdot e)\cdot 28^2]\sim 4.75$ nats plus an additional entropy due to a constant baseline with $a = 0.00028$ giving $-180\cdot 0.00028\cdot\ln(0.00028)\sim 0.41$ nats. The total S for compact islands is therefore ~ 5.16 nats. This value is slightly larger (6%) than the calculated one—see Equation S7 in Supplementary Materials—because of the differential entropy, used for a continuous variable, approximates the exact solution of the Shannon entropy used for a discrete variable; (right panel) in average $a = 0.0055$ therefore $-180\cdot 0.0055\cdot\ln(0.0055)\sim 5.15$ nats. Both are within the S range 0 and $\sim\ln(180)\sim 5.2$ nats).

Regardless of the pdf shape, a constant baseline is always present or, in other words, α has always a probability different from 0 to undertake all possible angles in the range $[0, 180]$ degree. Such probability depends on the island shape: small baseline for compact islands and vice versa—high baseline for dendritic islands (see caption of Figure 5). In agreement with D_f measurements, T_S promotes more dendritic islands and larger pdf baselines at 50 °C rather than at 25 °C.

As shown in the Supplementary Materials, S depends on the average islands size A_{px} (in px, i.e., the average number of pixels included in each island) and its value saturates after the critical size $A_{px} = 190$ px at this scan-size (1024×563 px², 6.0×3.3 μm²). Additionally, 6T islands at early stages of the growth, i.e., $\Theta = 0.25$ ML, have A_{px} of ~ 200 px and ~ 440 px for 25 and 50 °C, respectively. These average areas permit to deem S stable.

As shown in Figure 6, the differential entropy S depends on both Θ and T_S , growing faster in the first ML, and then saturating in the next MLs. Data are empirically fitted with the exponential *plateau* function:

$$S = S_{sat} - \Delta S \cdot e^{-\frac{\Theta - \Theta_T}{\Theta_C}} \quad (2)$$

where S_{sat} is the saturation value of S , $\Delta S = S_{sat} - S_0$ where S_0 is the initial islands entropy, Θ_C is the thickness constant, and Θ_T is a horizontal offset (plot translation). As explained in the Supplementary Materials, S is a scale-dependent parameter and S_0 is the initial islands entropy at a given scale-size, i.e., the differential entropy correspondent to the constant baseline. Strictly speaking, $S \rightarrow 0$ when island average area tends to 0. Therefore, S_0 cannot be the differential entropy at $\Theta = 0$, i.e., when there are not molecules deposited on the surface. As the average area of islands is reduced, their contours tend to be circular and smaller in length, thus S decreases. Accordingly, plots of Figure 6 are expected to shift towards x -axis due to progressively smaller S_{sat} and S_0 .

The saturation value of S is lower than ~ 5.2 nats, the maximum entropy for this system, for both T_S (see Table 1). As expected, S saturates at a higher value for a higher T_S because islands are more dendritic, hence they are less dendritic at 25 °C.

Table 1. Data extracted from exponential *plateau* fitting by using Equation (2).

T_S (°C)	S_{sat} (Nats)	S_0 (Nats)	Θ_C (ML)
25	(5.14 ± 0.02)	~3.80	(0.28 ± 0.08)
50	(5.186 ± 0.004)	~4.35	(0.38 ± 0.07)

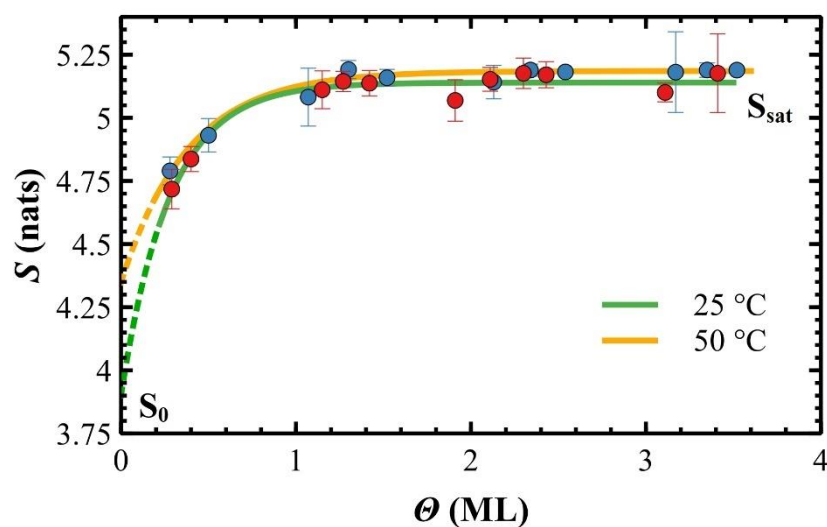


Figure 6. Data plots of S versus Θ at 25 and 50 °C fitted by an exponential *plateau* equation (Equation (2)).

In the exponential *plateau* model, the thickness constant Θ_C (in ML) describes how rapidly island shape, i.e., S , saturates for increasing deposited molecules. This process results faster at 50 °C rather than at 25 °C due to the increased diffusivity of molecules on the surface induced by T_S . In this empirical function, S reaches the 95% of the final asymptotical value when $\Theta = 3\Theta_C$, i.e., ~ 0.8 ML at 25 °C, and ~ 1.1 ML at 50 °C thus, in average, S saturates at ~ 0.9 ML that corresponds to the plot region where fitting curves are overlapped (see Figure 6). The large difference of S_0 for 25 and 50 °C (see Table 1) corresponds to compact or dendritic shapes, respectively (at the scan-size analysed in these experiments).

A graphical extrapolation of S_0 from fitting curves is clearly weak since it is supported by only two datapoint for each T_S (only two thickness Θ satisfy the experimental condition of separated islands at $\Theta < 1$ ML) and because the fitting function has the highest derivative at $\Theta = 0$.

Tentatively, the initial entropy S_0 could be dependent on the pdfs constant baselines. Averaging the constant baselines of pdfs sets (11 pdfs for each T_S), S_0 is (2.8 ± 1.1) nats for 25 °C and (3.2 ± 1.3) nats for 50 °C. These intervals include S_0 graphically extrapolated from fitting curves but, although more statistically relevant, this result is not supported by a theoretical explanation.

Since S and D_f are complexity measurements, a general monotonic positive relationship is expected. Figure 7 shows two distinctive regions for growing films fitted linearly: one correspondent to the first ML (green dashed line) and one for the other MLs up to the fourth one (red dashed line). In each region, independently on T_S (e.g., blue and purple data points in the first ML), entropy and fractal dimension are linearly correlated. Linear fits have two markedly different slopes: (i) in the early stage of the growth, data follow a linear trend with slope $\Delta S/\Delta D_f \approx 1$, so the entropy change has a one-to-one correspondence to the change of the island shape; (ii) in the next MLs, data collapse around a linear fit line almost horizontal to the x -axis with slope $\Delta S/\Delta D_f \approx 0.2$ thus, despite to a large variation in the island shape (D_f varies from ~ 1.35 to ~ 1.7), the island entropy changes slightly.

As reported in the literature [95–97], the angle entropy against the fractal dimension was used to discriminate physical/chemical parameters with different origins but, to date, a theoretical framework for explaining such correlations does not exist.

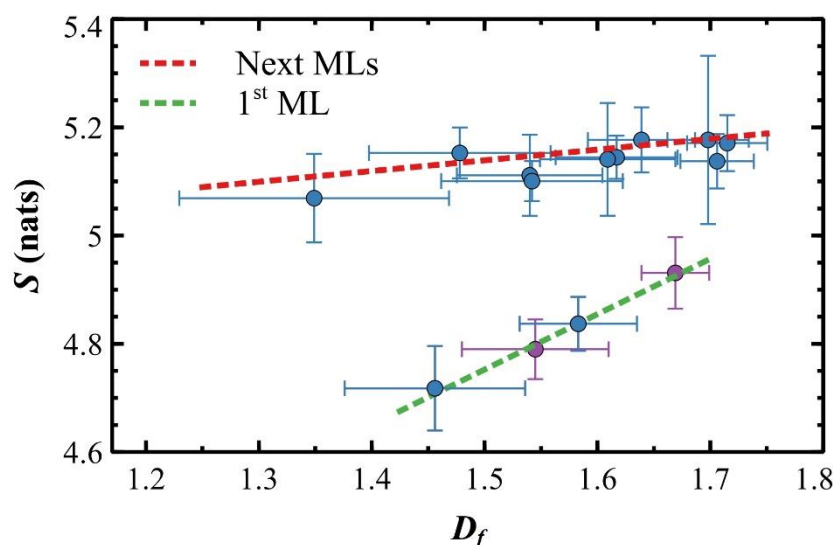


Figure 7. (Averaged) interfacial Shannon entropy S and fractal dimension D_f plot with fitted linear correlations. All the data were obtained from the AFM images at 25 °C and 50 °C, averaging the values obtained from all the single islands.

In 6T OTFs experiments, a tentative interpretation is possible, ascribing different slopes to different surface diffusion of 6T molecules on either native SiO_x or 6T MLs (cp. to Discussions section). According to OTF theory, surface diffusion energy depends on the diffusing layer: as reported in reference [98], diffusion of 6T molecules on native SiO_x involves a higher diffusion energy than for 6T molecules on a 6T ML (this is true also for next 6T MLs). A functional dependence of S versus D_f slope with respect to the diffusion energy is therefore expected and, specifically, the slope should be inversely related to the ease of diffusion of the molecules on the underneath layer.

4. Discussions

In general, the island shape is a result of the competition between two kinetic processes: edge diffusion and monomer incorporation [49]. Edge diffusion is characterized by the time taken by a monomer to diffuse along the island edge for finding an energetically favourable binding site. Monomer incorporation is characterized by the average time interval between two consecutive monomer incorporation events. The effect of frequent monomer incorporation is opposite to that of edge diffusion.

Islands formed in the DLA regime are taken as a reference system for the island growth. The monomer incorporation in the DLA regime is faster than the edge diffusion, leading to growth instabilities and fractal island shapes [44].

Both the incoming monomer flux, i.e., the deposition rate, and the surface area accessible to monomers via surface diffusion [99] determine the island growth rate at an island edge site. Monomer incorporation is enhanced by high flux, while the surface diffusion is characterized by a diffusion length determined by Voronoi tessellation [38]. Dendritic and fractal islands are formed when the diffusion length of monomers is small and islands are largely separated whereas, at the opposite (viz large diffusion length and small separation), compact or dendritic islands are formed. In the DLA growth, where fractal islands form, long protruding branches are associated with largely separated islands and a small diffusion length.

Based on the possibilities described in the aforementioned scenario, the island shape is modulated by both substrate and deposition rate. Specifically, largely separated islands are obtained on hydrophobic substrates that interact less with monomers, enabling their diffusion on the substrate surface (large diffusion length) [100]. The H passivated Si(111), H-Si(111), is an example of *quasi* hydrophobic substrate employed in organic growth experiments [49]. The chemical passivation of Si(111) produces a less hydrophilic surface

with a contact angle (CA) of 81 ± 2 degree [101], close to hydrophobic limit (90 degree). On the other hand, small islands slightly separated or large islands largely separated are formed on the SiO_2 surface if the deposition rate is relatively high or low, respectively.

As the growth proceeds, bricks of Voronoi tessellation including neighbouring islands begin to overlap. Monomers landing in the overlapping region have equal probability of being captured by either of the islands. This reduces the supply of monomers to each island, and limits further extension of fractal branches. A similar mechanism was proposed by Pratontep et al. [38] to explain the compact shape observed at relatively high deposition rates.

The 6T growth discussed in this work utilises a native SiO_x substrate that is more hydrophilic (CA = 58 ± 2 degree) than H-Si(111). Hence, as proved in reference [49], an increased island density is expected. The island density is also increased by the geometrical configuration of the in situ UHV system because of the OME cell has an angle of 60° with respect to the unit vector normal to the substrate plane. This inclination increases the effective deposition rate on the substrate by a factor ~ 10 in comparison to an OME cell *quasi* orthogonal to the substrate (12° in standard UHV flanges, see Supplementary Materials). The combination of these two effects causes a higher island density, i.e., $\sim 22 \mu\text{m}^{-2}$ at 25°C and $\sim 15 \mu\text{m}^{-2}$ at 50°C , compared to the ones reported in reference [49] ($\sim 1.5 \times 10^{-3} \mu\text{m}^{-2}$ on H-Si(111) and $\sim 4.5 \times 10^{-2} \mu\text{m}^{-2}$ SiO_2). A higher island density provokes the overlap of neighbouring bricks thus promoting a compact or dendritic island shape.

Regardless T_S , the trend of island shapes (D_f) across MLs is homogeneous although a difference between native SiO_x and 6T layers is morphologically clear. As shown in Figure 4, 6T islands at the native SiO_x interface evolves from compact to dendritic shape for increasing deposited molecules. The literature on similar experiments performed with organic and inorganic materials is contradictory: some results agree with the shape evolution therein described [42,82,102,103], in others is observed the opposite, i.e., islands evolve from dendritic to compact shape [85,86,88,104].

Two theoretical works explain our observations considering both the presence of other islands deposited on a substrate with a moderate diffusion length [44] and relatively small value of the ratio D/F where D is the diffusion rate of monomers on the surface and F is the molecular flux (i.e., the deposition rate) [105]. In 6T experiments, the hydrophilic native SiO_x substrate reduces the diffusion length (i.e., D) whereas a high deposition rate increases the island density (presence of other islands) and reduces the ratio D/F . Accordingly, monomer incorporation is favoured with respect to edge diffusion along the molecular deposition, so the island shape evolves from compact to dendritic.

The evolution of island shape observed on native SiO_x is kept for all 6T MLs. In the next layers, D_f increases slightly for comparable partial surface coverage Θ_p (see Figure 4). As described above, the second ML grows following the FM growth mode. As well as the native SiO_x substrate, a complete 6T ML has a CA = (57 ± 1) degree [37,106], therefore the diffusion length can be assumed comparable with the one on native SiO_x . Conversely, the island density is reduced to $\sim 6 \mu\text{m}^{-2}$ at 25°C and $\sim 3 \mu\text{m}^{-2}$ at 50°C . Being the islands more separated, a dendritic shape is favoured with respect to compact.

After the second ML, the OTF proceeds to the VW growth mode. The progressive dendritic shape in the third and fourth MLs agrees to the schematic of Luo et al. [47] where the ESB self-limits the underlayer islands promoting a more dendritic (even fractal) shape.

This shape evolution is similar for both T_S , although, at higher temperatures, islands are more dendritic (see Figure 4). This is clearly enhanced by the increase in surface diffusion, faster at 50°C than at 25°C , in agreement to Pimpinelli's work, demonstrating that islands tend to be dendritic (or fractal) if, and only if, the edge diffusion is much slower than the surface one [107].

As shown in Figure 7, the differential entropy S evolves linearly with island shapes. This is not the first time where a linear correlation between Shannon entropy and fractal dimension was found. Chen and coworkers [108], for instance, studied city spatial distributions and, defining Shannon entropy through a box counting method, were able to find the

same linear relationship. Following Figure 7, linear fits have a significant slope for the first ML whereas it is almost null for the next MLs. In the first ML, D_f shifts from ~ 1.5 to ~ 1.66 (average values for 25 and 50 °C) with an entropy increase of 0.5 nats. For the next MLs, D_f varies largely whereas S fluctuations are not significant (within ~ 0.1 nats for all MLs). As mentioned above, the D_f change reflects an increase in the complexity of the island contour: a very simple contour would be a low D_f that, conversely, increases for a very complex one. On the other hand, a change in S defines qualitatively the ‘roundness’ of finer details of the contour: e.g., for two S values, the lower one indicates a more circular contour, while the higher one corresponds to a more complex one, more difficult to be defined in a polar coordinate system (see Supplementary Materials).

The cartoon of Figure 8 sketches the relationship between S and D_f in Figure 7, where finer details of the contour and island shapes replace S and D_f , respectively.

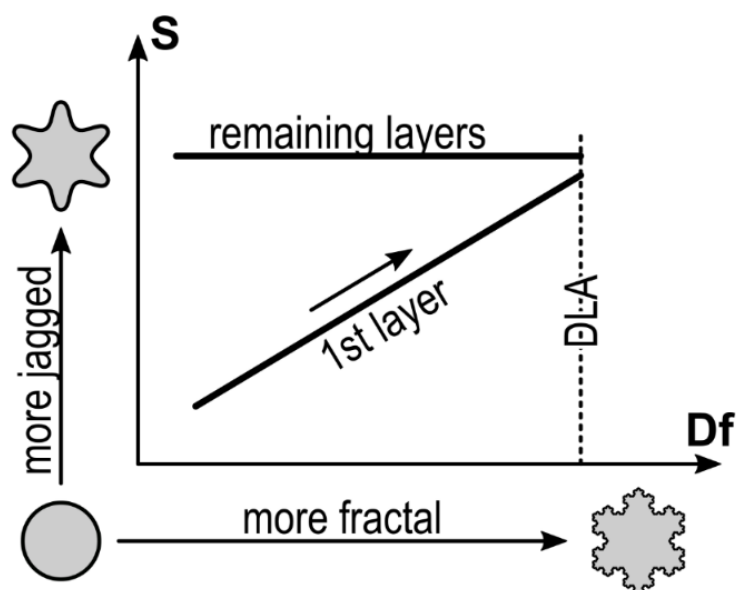


Figure 8. Qualitative interpretation of the geometric evolution of the island shape in terms of fractal dimension (x -axis) and differential entropy (y -axis) reported in Figure 7. The growth of the first (mono) layer is dictated by an initial formation of smooth circular islands, that progressively lose the circular symmetry and the contour becomes rougher (S increases due to a more jagged contour). The initial compact shape of the islands in the next MLs (remaining layers) is driven by the underneath 6T ML, that promotes a dendritic/fractal shape so that the initial circular symmetry is never recovered.

The differential entropy S in the y -axis shows an island with a circular contour at the inferior end that evolves into an island with comparable area but a more jagged contour at the superior end. On the other hand, the same island moves from compact to a dendritic/fractal shape in the x -axis. Such cartoon oversimplifies the differential entropy interpretation but suggests a geometrical interpretation of it: an increase in S is not only due to a polar symmetry loss moving from smooth to jagged contours. The roughness (fractality) of islands certainly increases S as proved by the entropy saturation obtained for higher D_f (cp. Figures 4 and 6).

Based on this scheme, the geometrical evolution of the island contour for increasing deposited molecules can be summarized as follows. At the early stage of the growth, compact islands form, with a smooth contour resulting in a relatively low value of both D_f and S . As the coverage Θ increases, the island contour of the first ML slowly loses the polar symmetry while the contour roughness increases in reason of the monomer incorporation as inferred by the D_f evolution. Progressively, islands reach a dendritic shape with D_f close to the DLA value (dashed vertical line) while S reaches its relative maximum value (cp. to Figure 6). At this point, the dendritic shape of the islands dominates with respect to finer

details of the contour highlighted by S . In the next MLs, the islands keep a dendritic shape ($D_f > 1.6$) with S slightly varying around an average value of 5.1, since finer contour details are hindered by the dendritic/fractal shape of the island. This condition is preserved up to the fourth ML because compact islands, where the effect of finer details is pronounced, do not form anymore.

Lastly, this result suggests an imprint effect on the growth induced by the underneath substrate: the native SiO_x does not impose any significant shape constrain to the first ML growth, while a 6T monolayer promotes a dendritic shape constrain.

5. Conclusions

In summary, a new method of analysis, based on differential entropy, is herein introduced to describe and interpret the shape complexity of self-similar organic islands. The differential entropy, which can be described as an “angle entropy”, is a parameter rarely exploited in diverse scientific fields. However, it shows a high sensitivity to finer details of the island contour. In situ Atomic Force Microscopy allows imaging step-by-step the growth of 6T islands while deposition proceeds. The evolution of the island shape for increasing thickness can be investigated computing fractal dimension and differential entropy. On well-separated thin film islands, the fractal dimension shows a linear correlation versus the film thickness and a high sensitivity to changes in the island shape, while the differential entropy saturates at the completion of the first monolayer. Remarkably, a linear correlation between differential entropy and fractal dimension is observed. This enables one to discern the 6T growth on native SiO_x or 6T layer and helps to link growth phenomena to the shape complexity indicating, for instance, how many molecules are needed to recover information entropy. Further experiments to classify islands, like in computing science [51], can be envisaged in order to provide a deeper geometrical perspective to growth phenomena. On the other hand, this approach needs a theoretical support for a correct interpretation of such phenomena. Finally, this work might boost new research on the Ehrlich-Schwoebel barrier, whose dependence on the fractal dimension of islands has been already proven [6].

Supplementary Materials: The following are available online at <https://www.mdpi.com/article/10.3390/ma14216529/s1>, Figure S1: Illustrative example of the box counting method, Figure S2: Steps to obtain polygonal chains describing the contour of the islands, Figure S3: Angle α between a segment and the radial line to the centroid of the island, Figure S4: Probability density functions of the angles α , Figure S5: Inkscape screenshot; Figure S6: Linear decreasing of δ versus Θ (in ML); Figure S7: Some pdfs related to growth steps with different islands configurations; Figure S8: Illustrative examples of—mostly—compact and—completely—dendritic islands affecting the absolute error on S ; Figure S9: Effect of the Scaling Factor; Figure S10: Two-level bitmap of synthetic images with circles, stars and dendritic islands; Figure S11: Plot of S (in nats) versus A_{px} (in px); Figure S12: Images and S analysis of synthetic filled David stars; Figure S13: Segmented image for circle with area $A_{px} \sim 60$ px; Figure S14: Contour of a circle quadrant for increasing size; Figure S15: Geometrical schemes of KCs versus substrate for in situ and ex situ OMBD systems. Table S1: Effect of the Scaling Factor (SF) on the differential entropy; Table S2: Effect of the island density (δ) on the differential entropy S ; Table S3: Effect of the image resolution (IR) on the differential entropy S .

Author Contributions: Conceptualization, S.C., P.S. and C.A.; methodology, P.S. and C.A.; software, P.S. and P.F.G.; validation, S.C., P.S. and C.A.; formal analysis, S.C.; investigation, S.C.; data curation, P.S. and C.A.; writing—original draft preparation, S.C., P.S. and C.A. All authors have read and agreed to the published version of the manuscript.

Funding: This research received no external funding.

Institutional Review Board Statement: Not applicable.

Informed Consent Statement: Not applicable.

Data Availability Statement: Python code is available in the website https://github.com/Cristiano1974a/Python_code.git (accessed on 25 August 2021) and distributed with GNU General Public License v3.0. The data presented in this study are available on request from the corresponding author.

Acknowledgments: Authors are grateful to Tobias Cramer for initial discussions on angle entropy and to Paolo Mei, Tiziano Bonfiglioli and Felice Carlo Simeone for helping them in the implementation of the UHV-AFM system. They are also indebted to Adrica Kyndiah and Franco Dinelli for proofreading the manuscript. Data were analysed by the GNU General Public Licensed software QtiPlot whereas most of figures are prepared with the GNU General Public Licensed software Veusz. AFM images were collected in the SPM@ISMN facility.

Conflicts of Interest: The authors declare no conflict of interest.

References

1. Dürr, A.C.; Schreiber, F.; Ritley, K.A.; Kruppa, V.; Krug, J.; Dosch, H.; Struth, B. Rapid Roughening in Thin Film Growth of an Organic Semiconductor (Diindenoperylene). *Phys. Rev. Lett.* **2003**, *90*, 16104. [[CrossRef](#)]
2. Zhang, X.N.; Barrera, E.; de Oteyza, D.G.; Dosch, H. Transition from layer-by-layer to rapid roughening in the growth of DIP on SiO₂. *Surf. Sci.* **2007**, *601*, 2420–2425. [[CrossRef](#)]
3. Frank, C.; Novák, J.; Banerjee, R.; Gerlach, A.; Schreiber, F.; Vorobiev, A.; Kowarik, S. Island size evolution and molecular diffusion during growth of organic thin films followed by time-resolved specular and off-specular scattering. *Phys. Rev. B* **2014**, *90*, 45410. [[CrossRef](#)]
4. Ehrlich, G.; Hudda, F.G. Atomic View of Surface Self-Diffusion: Tungsten on Tungsten. *J. Chem. Phys.* **1966**, *44*, 1039–1049. [[CrossRef](#)]
5. Schwoebel, R.L. Step Motion on Crystal Surfaces. II. *J. Appl. Phys.* **1969**, *40*, 614–618. [[CrossRef](#)]
6. Hlawacek, G.; Puschnig, P.; Frank, P.; Winkler, A.; Ambrosch Draxl, C.; Teichert, C. Characterization of step edge barriers in organic thin-film growth. *Science* **2008**, *321*, 108–111. [[CrossRef](#)]
7. Fendrich, M.; Krug, J. Ehrlich-Schwobel effect for organic molecules: Direct calculation of the step-edge barrier using empirical potentials. *Phys. Rev. B Condens. Matter Mater. Phys.* **2007**, *76*, 2–4. [[CrossRef](#)]
8. Goose, J.E.; First, E.L.; Clancy, P. Nature of step-edge barriers for small organic molecules. *Phys. Rev. B Condens. Matter Mater. Phys.* **2010**, *81*, 10–12. [[CrossRef](#)]
9. Zhang, X.; Barrera, E.; Goswami, D.; de Oteyza, D.G.; Weis, C.; Dosch, H. Evidence for a Layer-Dependent Ehrlich-Schwobel Barrier in Organic Thin Film Growth. *Phys. Rev. Lett.* **2009**, *103*, 136101. [[CrossRef](#)]
10. Biscarini, F.; Zamboni, R.; Samori, P.; Ostoja, P.; Taliani, C.; Samori, P.; Ostoja, P.; Taliani, C. Growth of conjugated oligomer thin films studied by atomic-force microscopy. *Phys. Rev. B* **1995**, *52*, 14868–14877. [[CrossRef](#)]
11. Virkar, A.A.; Mannsfeld, S.; Bao, Z.; Stingelin, N. Organic Semiconductor Growth and Morphology Considerations for Organic Thin-Film Transistors. *Adv. Mater.* **2010**, *22*, 3857–3875. [[CrossRef](#)]
12. Verlaak, S.; Steudel, S.; Heremans, P.; Heremans, P.; Janssen, D.; Janssen, D.; Deleuze, M.S. Nucleation of organic semiconductors on inert substrates. *Phys. Rev. B* **2003**, *68*, 195409. [[CrossRef](#)]
13. Riede, M.; Mueller, T.; Tress, W.; Schueppel, R.; Leo, K. Small-molecule solar cells—Status and perspectives. *Nanotechnology* **2008**, *19*, 424001. [[CrossRef](#)]
14. Fratini, S.; Nikolka, M.; Salleo, A.; Schweicher, G.; Sirringhaus, H. Charge transport in high-mobility conjugated polymers and molecular semiconductors. *Nat. Mater.* **2020**, *19*, 491–502. [[CrossRef](#)] [[PubMed](#)]
15. Dinelli, F.; Murgia, M.; Levy, P.; Cavallini, M.; Biscarini, F.; de Leeuw, D.M. Spatially Correlated Charge Transport in Organic Thin Film Transistors. *Phys. Rev. Lett.* **2004**, *92*, 90–93. [[CrossRef](#)] [[PubMed](#)]
16. Shehu, A.; Quiroga, S.D.; D’Angelo, P.; Albonetti, C.; Borgatti, F.; Murgia, M.; Scorzoni, A.; Stoliar, P.; Biscarini, F. Layered Distribution of Charge Carriers in Organic Thin Film Transistors. *Phys. Rev. Lett.* **2010**, *104*, 246602. [[CrossRef](#)] [[PubMed](#)]
17. Kyndiah, A.; Cramer, T.; Albonetti, C.; Liscio, F.; Chiodini, S.; Murgia, M.; Biscarini, F. Charge Transfer and Percolation in C₆₀/Pentacene Field-Effect Transistors. *Adv. Electron. Mater.* **2015**, *1*, 1400036. [[CrossRef](#)]
18. Liscio, F.; Albonetti, C.; Broch, K.; Shehu, A.; Quiroga, S.D.; Ferlauto, L.; Frank, C.; Kowarik, S.; Nervo, R.; Gerlach, A.; et al. Molecular reorganization in organic field-effect transistors and its effect on two-dimensional charge transport pathways. *ACS Nano* **2013**, *7*, 1257–1264. [[CrossRef](#)] [[PubMed](#)]
19. Chiodini, S.; Straub, A.; Donati, S.; Albonetti, C.; Borgatti, F.; Stoliar, P.; Murgia, M.; Biscarini, F. Morphological Transitions in Organic Ultrathin Film Growth Imaged by In Situ Step-by-Step Atomic Force Microscopy. *J. Phys. Chem. C* **2020**, *124*, 14030–14042. [[CrossRef](#)]
20. Brillante, A.; Bilotti, I.; Della Valle, R.G.; Venuti, E.; Girlando, A.; Masino, M.; Liscio, F.; Milita, S.; Albonetti, C.; D’angelo, P.; et al. Structure and dynamics of pentacene on SiO₂: From monolayer to bulk structure. *Phys. Rev. B* **2012**, *85*, 195308. [[CrossRef](#)]
21. Hlawacek, G.; Teichert, C. Nucleation and growth of thin films of rod-like conjugated molecules. *J. Phys. Condens. Matter* **2013**, *25*, 143202. [[CrossRef](#)]
22. Moulin, J.-F.F.; Dinelli, F.; Massi, M.; Albonetti, C.; Kshirsagar, R.; Biscarini, F. In situ X-ray synchrotron study of organic semiconductor ultra-thin films growth. *Nucl. Instrum. Methods Phys. Res. Sect. B Beam Interact. Mater. At.* **2006**, *246*, 122–126. [[CrossRef](#)]
23. Albonetti, C.; Barbalinardo, M.; Milita, S.; Cavallini, M.; Liscio, F.; Moulin, J.-F.; Biscarini, F. Selective Growth of alpha-Sexithiophene by Using Silicon Oxides Patterns. *Int. J. Mol. Sci.* **2011**, *12*, 5719–5735. [[CrossRef](#)]

24. Fritz, S.E.; Martin, S.M.; Frisbie, C.D.; Ward, M.D.; Toney, M.F. Structural Characterization of a Pentacene Monolayer on an Amorphous SiO₂ Substrate with Grazing Incidence X-ray Diffraction. *J. Am. Chem. Soc.* **2004**, *126*, 4084–4085. [[CrossRef](#)]
25. Mayer, A.C.; Ruiz, R.; Headrick, R.L.; Kazimirov, A.; Malliaras, G.G. Early stages of pentacene film growth on silicon oxide. *Org. Electron.* **2004**, *5*, 257–263. [[CrossRef](#)]
26. Mayer, A.C.; Ruiz, R.; Zhou, H.; Headrick, R.L.; Kazimirov, A.; Malliaras, G.G. Growth dynamics of pentacene thin films: Real-time synchrotron x-ray scattering study. *Phys. Rev. B* **2006**, *73*, 205307. [[CrossRef](#)]
27. Ruiz, R.; Choudhary, D.; Nickel, B.; Toccoli, T.; Chang, K.C.; Mayer, A.C.; Clancy, P.; Blakely, J.M.; Headrick, R.L.; Iannotta, S.; et al. Pentacene thin film growth. *Chem. Mater.* **2004**, *16*, 4497–4508. [[CrossRef](#)]
28. Krug, J.; Spohn, H. Universality classes for deterministic surface growth. *Phys. Rev. A* **1988**, *38*, 4271–4283. [[CrossRef](#)] [[PubMed](#)]
29. Valle, F.; Brucale, M.; Chiodini, S.; Bystrenova, E.; Albonetti, C. Nanoscale morphological analysis of soft matter aggregates with fractal dimension ranging from 1 to 3. *Micron* **2017**, *100*, 60–72. [[CrossRef](#)] [[PubMed](#)]
30. Kowarik, S.; Gerlach, A.; Sellner, S.; Schreiber, F.; Cavalcanti, L.; Kononov, O. Real-Time Observation of Structural and Orientational Transitions during Growth of Organic Thin Films. *Phys. Rev. Lett.* **2006**, *96*, 125504. [[CrossRef](#)]
31. Krause, B.; Dürr, A.C.; Ritley, K.; Schreiber, F.; Dosch, H.; Smilgies, D. Structure and growth morphology of an archetypal system for organic epitaxy: PTCDA on Ag(111). *Phys. Rev. B* **2002**, *66*, 235404. [[CrossRef](#)]
32. Yim, S.; Jones, T.S. Anomalous scaling behavior and surface roughening in molecular thin-film deposition. *Phys. Rev. B* **2006**, *73*, 161305. [[CrossRef](#)]
33. Zorba, S.; Shapir, Y.; Gao, Y. Fractal-mound growth of pentacene thin films. *Phys. Rev. B* **2006**, *74*, 245410. [[CrossRef](#)]
34. Evans, J.W.; Thiel, P.A.; Bartelt, M.C. Morphological evolution during epitaxial thin film growth: Formation of 2D islands and 3D mounds. *Surf. Sci. Rep.* **2006**, *61*, 1–128. [[CrossRef](#)]
35. Biscarini, F.; Samorì, P.; Greco, O.; Zamboni, R. Scaling Behavior of Anisotropic Organic Thin Films Grown in High Vacuum. *Phys. Rev. Lett.* **1997**, *78*, 2389–2392. [[CrossRef](#)]
36. Țălu, Ș. *Micro and Nanoscale Characterization of Three Dimensional Surfaces: Basics and Applications*; Napoca Star: Cluj-Napoca, Romania, 2015; ISBN 6066903497.
37. Chiodini, S.; D’Avino, G.; Muccioli, L.; Bartolini, L.; Gentili, D.; Toffanin, S.; Albonetti, C. Self-organization of complete organic monolayers via sequential post-deposition annealing. *Prog. Org. Coat.* **2020**, *138*, 105408. [[CrossRef](#)]
38. Pratontep, S.; Brinkmann, M.; Nüesch, F.; Zuppiroli, L. Correlated growth in ultrathin pentacene films on silicon oxide: Effect of deposition rate. *Phys. Rev. B* **2004**, *69*, 165201. [[CrossRef](#)]
39. Brinkmann, M.; Pratontep, S.; Contal, C. Correlated and non-correlated growth kinetics of pentacene in the sub-monolayer regime. *Surf. Sci.* **2006**, *600*, 4712–4716. [[CrossRef](#)]
40. Pratontep, S.; Nüesch, F.; Zuppiroli, L.; Brinkmann, M. Comparison between nucleation of pentacene monolayer islands on polymeric and inorganic substrates. *Phys. Rev. B* **2005**, *72*, 85211. [[CrossRef](#)]
41. Ruiz, R.; Nickel, B.; Koch, N.; Feldman, L.C.; Haglund, R.F.; Kahn, A.; Family, F.; Scoles, G.; Haglund, R.F., Jr.; Kahn, A.; et al. Dynamic Scaling, Island Size Distribution, and Morphology in the Aggregation Regime of Submonolayer Pentacene Films. *Phys. Rev. Lett.* **2003**, *91*, 136102. [[CrossRef](#)]
42. Ruiz, R.; Nickel, B.; Koch, N.; Feldman, L.C.; Haglund, R.F.; Kahn, A.; Scoles, G. Pentacene ultrathin film formation on reduced and oxidized Si surfaces. *Phys. Rev. B Condens. Matter Mater. Phys.* **2003**, *67*, 125406. [[CrossRef](#)]
43. Meyer zu Heringdorf, F.-J.J.; Reuter, M.C.; Tromp, R.M. Growth dynamics of pentacene thin films. *Nature* **2001**, *412*, 517–520. [[CrossRef](#)]
44. Bales, G.S.; Chrzan, D.C. Transition from Compact to Fractal Islands during Submonolayer Epitaxial Growth. *Phys. Rev. Lett.* **1995**, *74*, 4879–4882. [[CrossRef](#)]
45. Amar, J.G.; Semaan, M. Island nucleation and growth with anomalous diffusion. *Phys. Rev. E* **2016**, *93*, 062805. [[CrossRef](#)]
46. Liu, H.; Lin, Z.; Zhigilei, L.V.; Reinke, P. Fractal structures in fullerene layers: Simulation of the growth process. *J. Phys. Chem. C* **2008**, *112*, 4687–4695. [[CrossRef](#)]
47. Luo, Y.; Wang, G.; Theobald, J.A.; Beton, P.H. Fractal-compact island transition and self-limiting growth of pentacene on polymers. *Surf. Sci.* **2003**, *537*, 241–246. [[CrossRef](#)]
48. Royston, J.; Amar, J.G. Island-size distribution and capture numbers in three-dimensional nucleation: Dependence on island morphology. *Phys. Rev. E Stat. Nonlinear Soft Matter Phys.* **2009**, *80*, 041602. [[CrossRef](#)]
49. Huang, W.J.; Li, B.Q.; Zuo, J.M. Diffusion-limited submonolayer pentacene thin film growth on hydrogen-passivated Si(1 1 1) substrates. *Surf. Sci.* **2005**, *595*, 157–164. [[CrossRef](#)]
50. Zhu, W.; Mohammadi, E.; Diao, Y. Quantitative Image Analysis of Fractal-Like Thin Films of Organic Semiconductors. *J. Polym. Sci. Part B Polym. Phys.* **2019**, *57*, 1622–1634. [[CrossRef](#)]
51. Chambers, E.; Emerson, T.; Grimm, C.; Leonard, K. Exploring 2D Shape Complexity BT. In *Research in Shape Analysis: WiSH2, Sirince, Turkey, June 2016*; Genctav, A., Leonard, K., Tari, S., Hubert, E., Morin, G., El-Zehiry, N., Chambers, E., Eds.; Springer International Publishing: New York, NY, USA, 2018; pp. 61–83. ISBN 9783319770666.
52. Chen, Y.; Sundaram, H. Estimating Complexity of 2D Shapes. In Proceedings of the 2005 IEEE 7th Workshop on Multimedia Signal Processing, Shanghai, China, 30 October–2 November 2005; pp. 1–4.
53. Su, H.; Bouridane, A.; Crookes, D. Scale Adaptive Complexity Measure of 2D Shapes. In Proceedings of the 18th International Conference on Pattern Recognition (ICPR’06), Hong Kong, China, 20–24 August 2006; Volume 2, pp. 134–137.

54. Shannon, C.E. A mathematical theory of communication. *Bell Syst. Tech. J.* **1948**, *27*, 379–423. [[CrossRef](#)]
55. Shannon, C.E. Communication In The Presence Of Noise. *Proc. IEEE* **1998**, *86*, 447–457. [[CrossRef](#)]
56. Kish, L.B.; Ferry, D.K. Information entropy and thermal entropy: Apples and oranges. *J. Comput. Electron.* **2018**, *17*, 43–50. [[CrossRef](#)]
57. Çengel, Y.A. On Entropy, Information, and Conservation of Information. *Entropy* **2021**, *23*, 779. [[CrossRef](#)] [[PubMed](#)]
58. Jaynes, E.T. Information Theory and Statistical Mechanics. II. *Phys. Rev.* **1957**, *108*, 171–190. [[CrossRef](#)]
59. Jaynes, E.T. Information Theory and Statistical Mechanics. *Phys. Rev.* **1957**, *106*, 620–630. [[CrossRef](#)]
60. Castro-Alvaredo, O.A.; Doyon, B. Entanglement Entropy of Highly Degenerate States and Fractal Dimensions. *Phys. Rev. Lett.* **2012**, *108*, 120401. [[CrossRef](#)] [[PubMed](#)]
61. Dahlsten, O.C.O. Non-Equilibrium Statistical Mechanics Inspired by Modern Information Theory. *Entropy* **2013**, *15*, 5346–5361. [[CrossRef](#)]
62. Main, I.G.; Al-Kindy, F.H. Entropy, energy, and proximity to criticality in global earthquake populations. *Geophys. Res. Lett.* **2002**, *29*, 24–25. [[CrossRef](#)]
63. Arzate-Vázquez, I.; Chanona-Pérez, J.J.; Calderón-Domínguez, G.; Terres-Rojas, E.; Garibay-Febles, V.; Martínez-Rivas, A.; Gutiérrez-López, G.F. Microstructural characterization of chitosan and alginate films by microscopy techniques and texture image analysis. *Carbohydr. Polym.* **2012**, *87*, 289–299. [[CrossRef](#)]
64. Sitges, C.; Bornas, X.; Llabrés, J.; Noguera, M.; Montoya, P. Linear and nonlinear analyses of EEG dynamics during non-painful somatosensory processing in chronic pain patients. *Int. J. Psychophysiol.* **2010**, *77*, 176–183. [[CrossRef](#)]
65. Nemcsics, Á.; Nagy, S.; Mojzes, I.; Schwedhelm, R.; Woedtke, S.; Adelung, R.; Kipp, L. Investigation of the surface morphology on epitaxially grown fullerene structures. *Vacuum* **2009**, *84*, 152–154. [[CrossRef](#)]
66. Zmeskal, O.; Dzik, P.; Vesely, M. Entropy of fractal systems. *Comput. Math. Appl.* **2013**, *66*, 135–146. [[CrossRef](#)]
67. Tumbek, L.; Gleichweit, C.; Zojer, K.; Winkler, A. Origin of the bimodal island size distribution in ultrathin films of para-hexaphenyl on mica. *Phys. Rev. B* **2012**, *86*, 85402. [[CrossRef](#)]
68. Pulker, H.; Pulker, H.K. *Coatings on Glass*; Elsevier: Amsterdam, The Netherlands, 1999; Volume 20, ISBN 0080525555.
69. Nanbu, K.; Watanabe, Y. Thickness distribution of films fabricated by the molecular beam epitaxy technique. *Vacuum* **1986**, *36*, 349–354. [[CrossRef](#)]
70. Mandelbrot, B. *The Fractal Geometry of Nature*; W.H. Freeman: New York, NY, USA, 1982; ISBN 9780716711865.
71. Avnir, D.; Biham, O.; Lidar, D.; Malcai, O. Is the Geometry of Nature Fractal? *Science* **1998**, *279*, 39–40. [[CrossRef](#)]
72. Imre, A.R. Artificial fractal dimension obtained by using perimeter—Area relationship on digitalized images. *Appl. Math. Comput.* **2006**, *173*, 443–449. [[CrossRef](#)]
73. Douketis, C.; Wang, Z.; Haslett, T.L.; Moskovits, M. Fractal character of cold-deposited silver films determined by low-temperature scanning tunneling microscopy. *Phys. Rev. B* **1995**, *51*, 11022–11031. [[CrossRef](#)]
74. Nečas, D.; Klapetek, P. Gwyddion: An open-source software for SPM data analysis. *Cent. Eur. J. Phys.* **2012**, *10*, 181–188. [[CrossRef](#)]
75. Amar, J.G.; Family, F.; Lam, P.-M. Dynamic scaling of the island-size distribution and percolation in a model of submonolayer molecular-beam epitaxy. *Phys. Rev. B* **1994**, *50*, 8781–8797. [[CrossRef](#)] [[PubMed](#)]
76. Schneider, C.A.; Rasband, W.S.; Eliceiri, K.W. NIH Image to ImageJ: 25 years of image analysis. *Nat. Methods* **2012**, *9*, 671–675. [[CrossRef](#)]
77. Michalowicz, J.V.; Nichols, J.M.; Bucholtz, F. Calculation of Differential Entropy for a Mixed Gaussian Distribution. *Entropy* **2008**, *10*, 200–206. [[CrossRef](#)]
78. Marsh, C. Introduction to Continuous Entropy. *Dep. Comput. Sci. Princet. Univ.* **2013**. Available online: https://www.crmmarsh.com/static/pdf/Charles_Marsh_Continuous_Entropy.pdf (accessed on 25 August 2021).
79. Inkscape Project Inkscape. Inkscape Project. Inkscape, 2020. Available online: <https://inkscape.org> (accessed on 25 August 2021).
80. Pratontep, S.; Brinkmann, M.; Nüesch, F.; Zuppiroli, L. Nucleation and growth of ultrathin pentacene films on silicon dioxide: Effect of deposition rate and substrate temperature. *Synth. Met.* **2004**, *146*, 387–391. [[CrossRef](#)]
81. Venables, J.A. *Introduction to Surface and Thin Film Processes*; Cambridge University Press: Cambridge, UK, 2000; ISBN 9780521785006.
82. Hwang, R.Q.; Schröder, J.; Günther, C.; Behm, R.J. Fractal growth of two-dimensional islands: Au on Ru(0001). *Phys. Rev. Lett.* **1991**, *67*, 3279–3282. [[CrossRef](#)] [[PubMed](#)]
83. Bérubé, D.; Jébrak, M. High precision boundary fractal analysis for shape characterization. *Comput. Geosci.* **1999**, *25*, 1059–1071. [[CrossRef](#)]
84. Bensimon, D.; Domany, E.; Aharony, A. Crossover of Fractal Dimension in Diffusion-Limited Aggregates. *Phys. Rev. Lett.* **1983**, *51*, 1394. [[CrossRef](#)]
85. Brune, H.; Bromann, K.; Kern, K.; Jacobsen, J.; Stoltze, P.; Jacobsen, K.; Nørskov, J. Fractal and Dendritic Growth of Surface Aggregates. *MRS Online Proc. Libr.* **1995**, *407*, 379–389. [[CrossRef](#)]
86. Yang, J.; Wang, T.; Wang, H.; Zhu, F.; Li, G.; Yan, D. Ultrathin-film growth of para-sexiphenyl (II): Formation of large-size domain and continuous thin film. *J. Phys. Chem. B* **2008**, *112*, 7821–7825. [[CrossRef](#)]
87. Batabyal, R.; Mahato, J.C.; Das, D.; Roy, A.; Dev, B.N. Self-organized one-atom thick fractal nanoclusters via field-induced atomic transport. *J. Appl. Phys.* **2013**, *114*, 64304. [[CrossRef](#)]

88. Yang, J.; Wang, T.; Wang, H.; Zhu, F.; Li, G.; Yan, D. Ultrathin-film growth of para-sexiphenyl (I): Submonolayer thin-film growth as a function of the substrate temperature. *J. Phys. Chem. B* **2008**, *112*, 7816–7820. [[CrossRef](#)] [[PubMed](#)]
89. Wu, Y.; Toccoli, T.; Zhang, J.; Koch, N.; Iacob, E.; Pallaoro, A.; Iannotta, S.; Rudolf, P. Key role of molecular kinetic energy in early stages of pentacene island growth. *Appl. Phys. A* **2009**, *95*, 21–27. [[CrossRef](#)]
90. Witten, T.A.; Sander, L.M. Diffusion-limited aggregation. *Phys. Rev. B* **1983**, *27*, 5686–5697. [[CrossRef](#)]
91. Garbaczewski, P. Differential Entropy and Dynamics of Uncertainty. *J. Stat. Phys.* **2006**, *123*, 315. [[CrossRef](#)]
92. Michalowicz, J.V.; Nichols, J.M.; Bucholtz, F. *Handbook of Differential Entropy*; CRC Press: Boca Raton, FL, USA, 2013; ISBN 1466583169.
93. Mac Fhionnlaoich, N.; Guldin, S. Information Entropy as a Reliable Measure of Nanoparticle Dispersity. *Chem. Mater.* **2020**, *32*, 3701–3706. [[CrossRef](#)]
94. Lazo, A.V.; Rathie, P. On the entropy of continuous probability distributions (Corresp.). *IEEE Trans. Inf. Theory* **1978**, *24*, 120–122. [[CrossRef](#)]
95. Li, Z.; Costa, L.D.F. Investigating shape and function relationship in retinal ganglion cells. *J. Integr. Neurosci.* **2002**, *01*, 195–215. [[CrossRef](#)]
96. Vařenka, J.; Kubinek, R. Image analysis tools of dendritic structure classification. *Pattern Recognit. Image Anal.* **2006**, *16*, 651–655. [[CrossRef](#)]
97. Andrlé, R. Complexity and scale in geomorphology: Statistical self-similarity vs. characteristic scales. *Math. Geol.* **1996**, *28*, 275–293. [[CrossRef](#)]
98. Chiodini, S. In-Situ and Real Time Scanning Probe Microscopy of Organic Ultra THIN films. Ph.D. Thesis, Università di Bologna, Bologna, Italy, 2015.
99. Mulheran, P.A.; Blackman, J.A. The origins of island size scaling in heterogeneous film growth. *Philos. Mag. Lett.* **1995**, *72*, 55–60. [[CrossRef](#)]
100. 3M Science Applied to Life. *Hydrophilicity and Surface Energy, a Little of the Science behind the Test Strip*; 3M Science Applied to Life: Saint Paul, MN, USA, 2018.
101. Dinelli, F.; Moulin, J.-F.; Loi, M.A.; Da Como, E.; Massi, M.; Murgia, M.; Muccini, M.; Biscarini, F.; Wie, J.; Kingshott, P. Effects of Surface Chemical Composition on the Early Growth Stages of α -Sexithienyl Films on Silicon Oxide Substrates. *J. Phys. Chem. B* **2006**, *110*, 258–263. [[CrossRef](#)]
102. Wu, Y.; Toccoli, T.; Koch, N.; Iacob, E.; Pallaoro, A.; Rudolf, P.; Iannotta, S. Controlling the Early Stages of Pentacene Growth by Supersonic Molecular Beam Deposition. *Phys. Rev. Lett.* **2007**, *98*, 076601. [[CrossRef](#)]
103. Tonezzer, M.; Rigo, E.; Gottardi, S.; Bettotti, P.; Pavesi, L.; Iannotta, S.; Toccoli, T. Role of kinetic energy of impinging molecules in the α -sexithiophene growth. *Thin Solid Film.* **2011**, *519*, 4110–4113. [[CrossRef](#)]
104. Huang, L.; Liu, C.; Yu, B.; Zhang, J.; Geng, Y.; Yan, D. Evolution of 2,5-Bis(4-biphenyl)bithiophene Thin Films and Its Effect on the Weak Epitaxy Growth of ZnPc. *J. Phys. Chem. B* **2010**, *114*, 4821–4827. [[CrossRef](#)]
105. Lee, S.B. Measure of the fractal dimension of islands in epitaxial thin film growth. *J. Korean Phys. Soc.* **2005**, *47*, 577.
106. Bartolini, L.; Malferrari, M.; Lugli, F.; Zerbetto, F.; Paolucci, F.; Pelicci, P.G.; Albonetti, C.; Rapino, S. Interaction of Single Cells with 2D Organic Monolayers: A Scanning Electrochemical Microscopy Study. *ChemElectroChem* **2018**, *5*, 2975–2981. [[CrossRef](#)]
107. Pimpinelli, A.; Villain, J.; Wolf, D.E. Fractal terraces in MBE growth. *J. Phys. I* **1993**, *3*, 447–457. [[CrossRef](#)]
108. Chen, Y.; Wang, J.; Feng, J. Understanding the Fractal Dimensions of Urban Forms through Spatial Entropy. *Entropy* **2017**, *19*, 600. [[CrossRef](#)]